

Journal of Materials Chemistry C

Accepted Manuscript



This is an *Accepted Manuscript*, which has been through the Royal Society of Chemistry peer review process and has been accepted for publication.

Accepted Manuscripts are published online shortly after acceptance, before technical editing, formatting and proof reading. Using this free service, authors can make their results available to the community, in citable form, before we publish the edited article. We will replace this *Accepted Manuscript* with the edited and formatted *Advance Article* as soon as it is available.

You can find more information about *Accepted Manuscripts* in the [Information for Authors](#).

Please note that technical editing may introduce minor changes to the text and/or graphics, which may alter content. The journal's standard [Terms & Conditions](#) and the [Ethical guidelines](#) still apply. In no event shall the Royal Society of Chemistry be held responsible for any errors or omissions in this *Accepted Manuscript* or any consequences arising from the use of any information it contains.

Understanding the Vapor-Liquid-Solid Mechanism of Si Nanowire Growth and Doping to Synthetically Encode Precise Nanoscale Morphology

*Christopher W. Pinion, Joseph D. Christesen, and James F. Cahoon**

Department of Chemistry, University of North Carolina at Chapel Hill, Chapel Hill, NC 27599-3290, United States

Abstract

Bottom-up, chemical methods to control the morphology of semiconductor nanostructures are a promising complement to the top-down fabrication techniques that currently dominate the semiconductor industry. Among bottom-up techniques, nanowire (NW) growth using the vapor-liquid-solid (VLS) mechanism has received great attention. In this Highlight article, we review our recent progress toward understanding the microscopic processes that govern VLS NW growth, doping, and dopant modulation. Quantitative measurements of Si NW growth rates and P dopant profiles under a range of synthetic conditions are interpreted with a kinetic analysis of VLS growth that includes the microscopic reactions of incorporation, evaporation, and crystallization. The analysis allows us to identify synthetic conditions that yield both diameter-independent growth rates and abrupt, diameter-independent dopant transitions. The optimized conditions allow precise, sub-10 nm morphology to be encoded along the growth axis of Si NWs, enabling the bottom-up chemical nanofabrication of complex structures that are typically fabricated by high-resolution, top-down lithography.

Keywords: bottom-up fabrication, nanoscale lithography, vapor-liquid-solid mechanism, silicon nanowire, phosphorus doping

Introduction

Precise patterning of semiconductor materials utilizing top-down lithographic techniques is integral to the advanced electronics we use on a daily basis. However, continuing development of these lithographic technologies often results in the trade-off of either high cost or low throughput, and three-dimensional (3D) patterning can be difficult to achieve.^{1,2} Bottom-up, chemical methods to control the 3D nanoscale morphology of semiconductor nanostructures have received significant attention as a complementary technique. Semiconductor nanowires (NWs) grown by the vapor-liquid-solid (VLS) mechanism are an especially promising platform because the wire composition can be modulated during growth and the high aspect ratio, one-dimensional structure enables integration in a range of devices.^{3,4} Although many NW-based technologies have been demonstrated, including photovoltaic devices,⁵⁻⁷ waveguides,^{8,9} sensors,¹⁰ and thermoelectrics,^{11,12} they have generally been limited by the cylindrical “wire” morphology and inability to create the diverse range of arbitrary structures and shapes routinely fabricated by top-down methods.

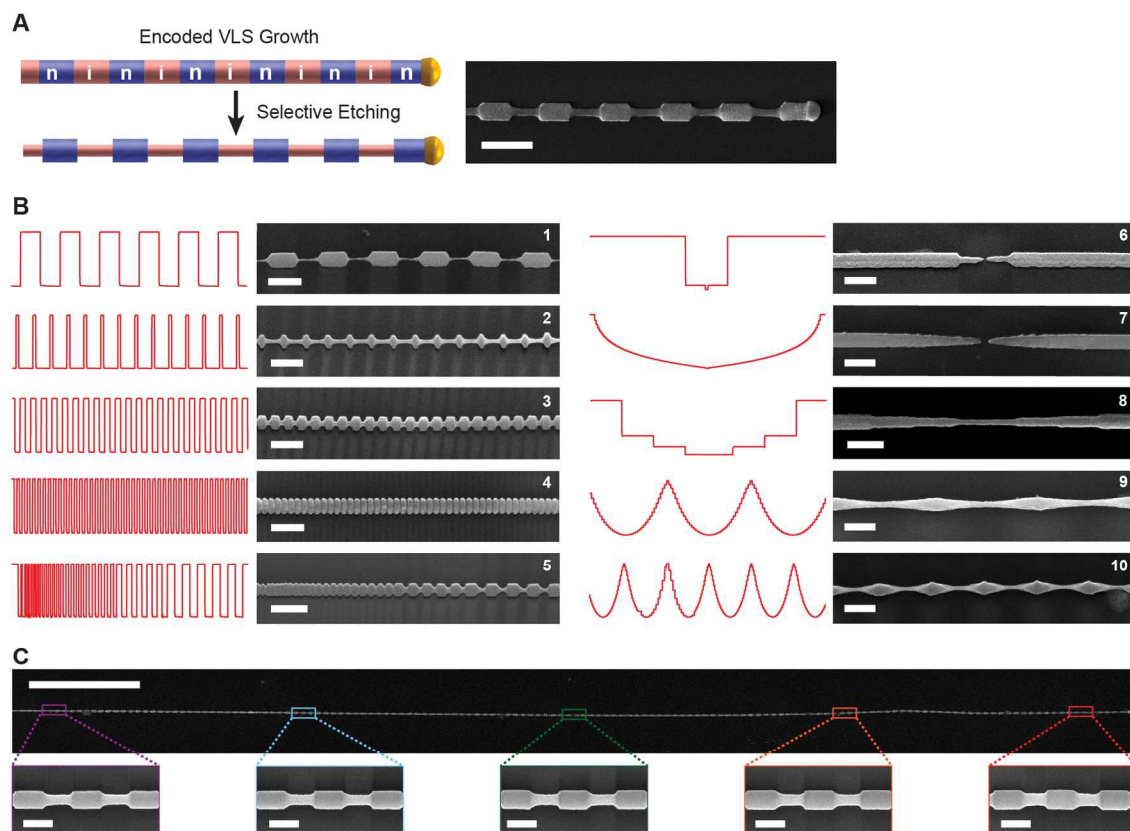


Figure 1. Encoding Complex 3D Morphology in Si NWs. (A) Left: Schematic illustration of NW growth including rapid modulation of P dopant incorporation to form heavily-doped n-type (n) and undoped intrinsic (i) segments that are selectively etched using wet-chemical methods to form a grating. Right: SEM image of a grating-enclosed nanowire; scale bar, 200 nm. (B) SEM images and phosphine flow profiles for the synthesis of Si NWs with complex morphology. The measured phosphine flow profile used to encode the morphology of each segment is depicted in red to the left of each SEM image; all scale bars, 200 nm. The flow rates vary from 0 to 20 sccm for each NW. (C) Upper: SEM image of a grating-enclosed NW more than 50 μm in axial length; scale bar, 5 μm . Lower: Higher magnification SEM images of select sections of the NW in the upper panel; scale bars, 200 nm. Adapted with permission from reference 13. Copyright 2013 American Chemical Society.

Recently, we developed a technique to synthetically encode arbitrary 3D morphology with sub-10 nm resolution in VLS-grown Si NWs.¹³ This technique, termed ENGRAVE for Encoded Nanowire Growth and Apppearance through VLS and Etching, is a two-step process, illustrated in Figure 1A, that leverages precise incorporation of P dopants during VLS growth and dopant-dependent, wet-chemical etching that selectively removes lightly-doped regions of the NW. As shown by the gallery of scanning electron microscopy (SEM) images in Figure 1B, the range of morphologies accessible by this technique is exceptionally diverse, including periodic (images 1-4) or asymmetric (image 5) gratings, nanogaps with gap sizes smaller than 10 nm (images 6-7), suspended nanorods (image 8), and sinusoidal profiles (images 9-10). Moreover, these structures can be encoded with high fidelity over length scales exceeding 50 microns, as illustrated by the SEM images in Figure 1C. Each type of NW structure can enable a new class of NW-based technology.¹⁴ Importantly, the precise control afforded by the ENGRAVE process allows rational design of nanostructures that are tailored to address specific scientific and technological challenges.

The fidelity of ENGRAVE structures is predicated on precise control over two aspects of NW growth. First, the NW growth rate must be uniformly controlled in order to encode segments of precisely-defined length. Second, the P doping level and the abruptness of dopant transitions must be controlled to precisely modulate the etch rate and thus morphology of a given segment. In this Highlight article, we review our recent progress on understanding the microscopic processes that facilitate VLS NW growth¹⁵ and doping,¹⁶ enabling high-fidelity ENGRAVE nanostructures.

VLS Growth Kinetics

As illustrated in Figure 2A, we utilized ENGRAVE as an analytical tool to probe VLS growth kinetics by encoding sequential n-type and intrinsic segments in NWs at a variety of temperatures (365-480 °C), SiH_4 partial pressures (0.1-1.6 Torr SiH_4) and NW diameters (30-200 nm). Quantitative SEM image analysis of wire segments from each distinct growth condition, as exemplified in Figure 2B, was used to produce a comprehensive set of NW growth rate data across more than 65 different synthetic conditions. NWs grew along the [111] or [112] directions; however, we speculate the effect of crystal direction on growth rate is minimal given the extremely narrow distributions of nanowire growth rates presented below.

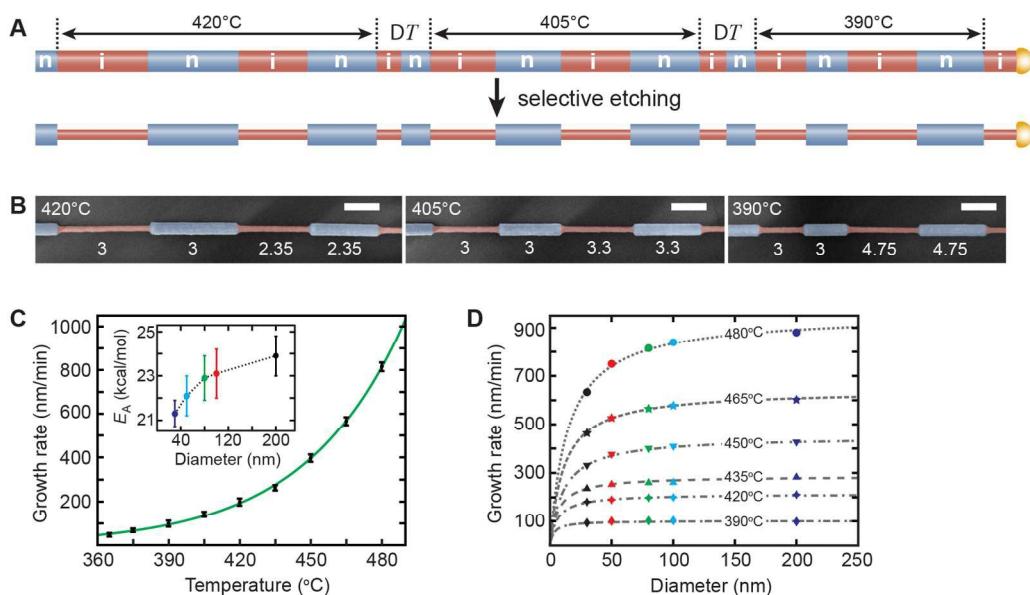


Figure 2. Determination of Si NW VLS Growth Kinetics. (A) Upper: Schematic illustration of alternating n-type (n) and intrinsic (i) segments encoded sequentially during VLS NW growth at temperatures of 420, 405, and 390 °C. Sections denoted ΔT are not drawn to scale and correspond to regions over which the temperature was lowered

at a rate of 1 °C/min. Lower: Illustration of the NW morphology that results from etching in aqueous KOH solution, which selectively removes intrinsic sections (red) of the NW.

(B) False-colored SEM images of a Si NW ~80 nm in diameter with sequential segments encoded at 420 (left), 405 (middle), and 390 °C (right). Growth times in minutes are

denoted beneath each segment, and all segments were grown at a SiH₄ partial pressure of 0.4 Torr and total pressure of 40 Torr; scale bars, 250 nm. Analysis of these type of SEM

images yielded quantitative temperature- and diameter-dependent growth rates. (C) Plot

of growth rate vs. temperature for NWs 80 nm in diameter grown with a SiH₄ partial pressure of 0.4 Torr; error bars reflect two standard deviations (2σ). The solid green line

represents a fit to the Arrhenius expression. Inset: activation energy as a function of NW diameter, as determined by fits to growth rate data for NWs 30 to 200 nm in diameter.

(D) NW growth rate as a function of diameter for temperatures of 390 (diamond), 420

(square), 435 (triangle), 450 (inverted triangle), 465 (star), and 480 °C (circle). Dashed

lines represent a fit of the data at each temperature using the equations developed in the

kinetic analysis.¹⁵ Adapted with permission from reference 15. Copyright 2014 American Chemical Society.

Temperature-dependent growth rate data from a single NW diameter (80 nm) at a single SiH₄ partial pressure (0.4 Torr) is depicted in Figure 2C and is representative of the data acquired at other synthetic conditions. The data is well fit to the Arrhenius expression and produces an activation energy of 22.9 ± 1.0 kcal/mol, which is in good agreement with literature values.¹⁷⁻²² Arrhenius plots were created for additional diameters and partial pressures (not shown), and, surprisingly, we observed a diameter-

dependent activation energy, as shown in the inset of Figure 2C. We attribute this diameter dependence to the enhanced catalytic activity of small diameter metal nanoparticles.^{23, 24} Although this effect produces a NW growth rate that depends on diameter, the magnitude is small compared to the diameter-dependent effects discussed later in the text (*e.g.* the Gibbs-Thomson effect) and thus can often be neglected.

Growth kinetics as a function of diameter for a variety of temperatures and a fixed SiH₄ partial pressure of 0.4 Torr are depicted in Figure 2D. For lower temperatures of 390 °C and below, we observed diameter-independent kinetics. In contrast, for higher temperatures of 435 °C and above, we observed an asymptotically increasing growth rate with increasing NW diameter. In a similar set of experiments at constant temperature (not shown here),¹⁵ we observed diameter-independent growth kinetics at low SiH₄ partial pressures and an asymptotically increasing growth rate with increasing NW diameter for high SiH₄ partial pressures. Thus, the experiments demonstrate that the growth rate can be diameter dependent or independent depending on both temperature and SiH₄ partial pressure.

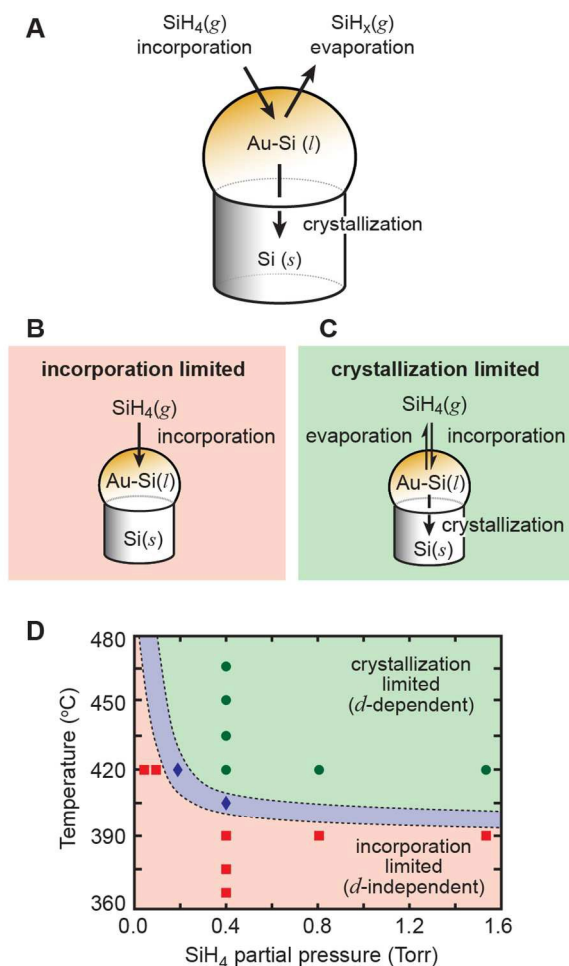


Figure 3. Kinetic Modeling of VLS NW Growth. (A) Illustration of the three key processes—incorporation, evaporation, and crystallization—that are used to model Si NW growth by the VLS mechanism. (B) Illustration of the key kinetic processes for the incorporation-limited (diameter-independent) regime, which is dominated by the rate of Si incorporation from the gas phase. (C) Illustration of the key kinetic processes for the crystallization-limited (diameter-dependent) regime, which includes rapid vapor-liquid equilibration and slower Si crystallization. (D) ‘Phase’ diagram depicting regions of temperature and silane partial pressure in which VLS growth is crystallization limited (shaded green), incorporation limited (shaded red), or intermediate (shaded blue). Red squares denote synthetic conditions with a diameter-independent growth rate, green

circles a diameter-dependent growth rate, and blue diamonds the transition between diameter-independent and diameter-dependent regimes. Adapted with permission from reference 15. Copyright 2014 American Chemical Society.

To interpret the growth rate data, we developed a kinetic analysis of the VLS growth mechanism considering the three simple microscopic processes—incorporation, evaporation, and crystallization—depicted in Figure 3A. In this framework, Si is supplied to the catalyst via the incorporation process, which consists of dissociative adsorption of SiH₄ gas on the catalyst surface and incorporation of Si into the liquid alloy. Si atoms may proceed through one of two reaction pathways once in the liquid alloy catalyst. The first pathway expels Si atoms from the catalyst as vapor-phase SiH_x species through associative desorption at the catalyst surface, which we refer to as the “evaporation” process. Alternatively, Si may be added to the solid NW at the solid-liquid interface via the crystallization process, which elongates the NW.

This kinetic analysis¹⁵ yielded an expression for the NW growth rate, G , of:

$$G \propto \frac{k_c k_i}{k_e + k_c/2} P, \quad (1)$$

where k_c , k_i and k_e are the rate constants for the crystallization, incorporation, and evaporation reactions, respectively, and P is the partial pressure of SiH₄ in the reactor. Equation 1 also assumes that the NW and liquid droplet diameters are equal, which introduces the factor of 2 in the denominator. The kinetic growth model assumes a constant partial pressure of vapor-phase precursors and thus does not account for depletion or diffusional effects that might occur under higher temperature and pressure conditions. A more comprehensive kinetic analysis would also include dissolution of

solid Si back into the liquid catalyst, a process important for the solid-liquid-vapor etching process.²⁵ However, in the current analysis, we assume the liquid catalyst is consistently supersaturated and assume that under these conditions the dissolution process can be accounted for in the effective rate constant for crystallization, k_c .

The temperature- and diameter-dependence of the NW growth rate (*cf.* Figure 2) arises through the three rate constants in equation 1. We assume that k_i can be described by the Arrhenius expression, producing the diameter-dependent activation energies shown in Figure 2C. A similar Arrhenius dependence might be expected for the crystallization reaction; however, we approximated k_c as temperature-independent over the relatively small temperature range used in this study because the energetic barrier to crystallization is expected to be substantially lower than the barrier to incorporation.²⁶ Finally, k_e is assumed to have an Arrhenius dependence on temperature and a dependence on d^{-1} , where d is the NW diameter. The dependence on inverse diameter arises from the Gibbs-Thomson effect, which increases the vapor pressure of Si species in small diameter catalysts because of the curved liquid surface.²⁷⁻³¹

Analysis of equation 1 produces two limiting cases with contrasting NW growth characteristics. First, for synthetic conditions where $k_c \gg 2k_e$, the growth rate becomes:

$$G \propto k_i P. \quad (2)$$

In this limit, the growth rate is expected to be diameter-independent because k_e does not appear in the expression. As illustrated schematically in Figure 3B, this limit may be considered an incorporation-limited regime because the growth rate only depends on k_i .

Second, for synthetic conditions where $k_c \ll 2k_e$, the growth rate becomes:

$$G \propto \frac{k_i k_c}{k_e} P. \quad (3)$$

In this limit, the growth rate is expected to be diameter-dependent because k_e appears in the denominator of the expression and carries the d^{-1} dependence. As illustrated schematically in Figure 3C, this limit may be considered a crystallization-limited regime because the relatively slower crystallization rate (because of a lower rate constant) induces a dynamic vapor-liquid equilibrium, which causes all three rate constants to appear in the expression for the growth rate.

The experimental growth rate data may be interpreted within the limits of the kinetic analysis presented above. Figure 3D depicts a “phase” diagram, in which the measured diameter dependence at various synthetic conditions (*cf.* Figure 2D) was used to classify the NW growth kinetics as either incorporation- or crystallization-limited. We observe incorporation-limited NW growth at low temperatures and SiH₄ partial pressures (red region), while crystallization-limited growth is observed at higher temperatures and SiH₄ partial pressures (green region). These mechanistic insights guide the choice of synthetic conditions to be used for ENGRAVE structures, for which a diameter-independent growth rate is preferred.

Dopant Modulation during VLS Growth

Precise control over dopant incorporation during VLS growth is required to optimize the abruptness of interfaces and create high resolution ENGRAVE structures. The synthesis of radially uniform doping and abrupt axial transitions in NW heterostructures has been a long-standing issues in the NW literature.³²⁻⁴² Non-uniform radial dopant profiles, showing for instance increased P concentration at the NW surface, can arise from vapor-solid (VS) overcoating. Broadened material transitions along the

wire growth axis can result from the ‘reservoir effect,’ in which the liquid catalyst acts a reservoir of material after the gas-phase precursor is removed.

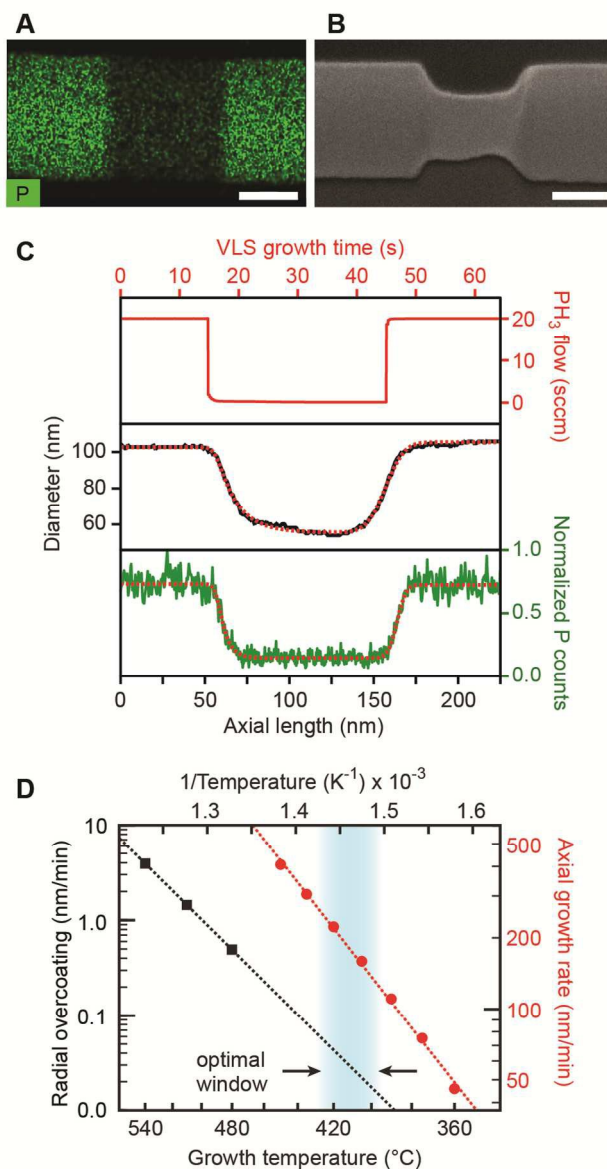


Figure 4. Evaluating and Modeling the Uniformity and Abruptness of P Dopant

Profiles. (A) EDS image, showing P counts in green, for an n-type/intrinsic/n-type wire with a ~ 100 nm intrinsic section; scale bar, 50 nm. (B) SEM image of a NW, grown under the same conditions as in panel A, after wet-chemical KOH etching; scale bar, 50

nm. (C) Top: PH₃ flow profile (red curve) in units of sccm for the n-type/intrinsic/n-type sections shown in panels A and B. Middle: diameter profile (black curve) derived from the SEM image in panel B and best fit¹⁶ (red dashed line). Bottom: P counts (green curve) derived from the EDS image in panel A and best fit¹⁶ (red dashed line). (D) Logarithmic plot of the axial VLS NW growth rate (red circles and right-hand axis) and the radial VS overcoating rate (black squares and left-hand axis) as a function of inverse temperature. Dashed lines represent the best fit to the Arrhenius expression, yielding an activation energy of 42 ± 3 kcal/mol for VS overcoating. Adapted with permission from reference 16. Copyright 2014 American Chemical Society.

We evaluated the uniformity and abruptness of the dopant distribution in ENGRAVE structures using a combination of energy dispersive x-ray (EDS) mapping in a scanning transmission electron microscope and SEM imaging following wet-chemical etching.¹⁶ A high resolution EDS map of the P-dopants in an n-type/intrinsic/n-type NW (Figure 4A), combined with a SEM image of the corresponding structure after etching (Figure 4B), show two distinct features. First, the dopants appear to be highly uniform in the radial direction. The radial uniformity results from the choice of a growth temperature, 420 °C, that minimizes vapor-solid overcoating on the wire surface while maintaining a reasonable axial growth rate, as shown by the Arrhenius plot in Figure 4D comparing the radial overcoating and axial growth rates. Second, the EDS map and the SEM image exhibit abrupt transitions with characteristic lengths of ~5 nm at the n-type/intrinsic as well as intrinsic/n-type transitions, as shown by the dopant and diameter profiles in Figure 4C. Surprisingly, these short transitions show none of the expected

broadening from the reservoir effect, which is known to produce material transitions on much longer length scales comparable to the NW diameter.^{32, 33, 36, 37}

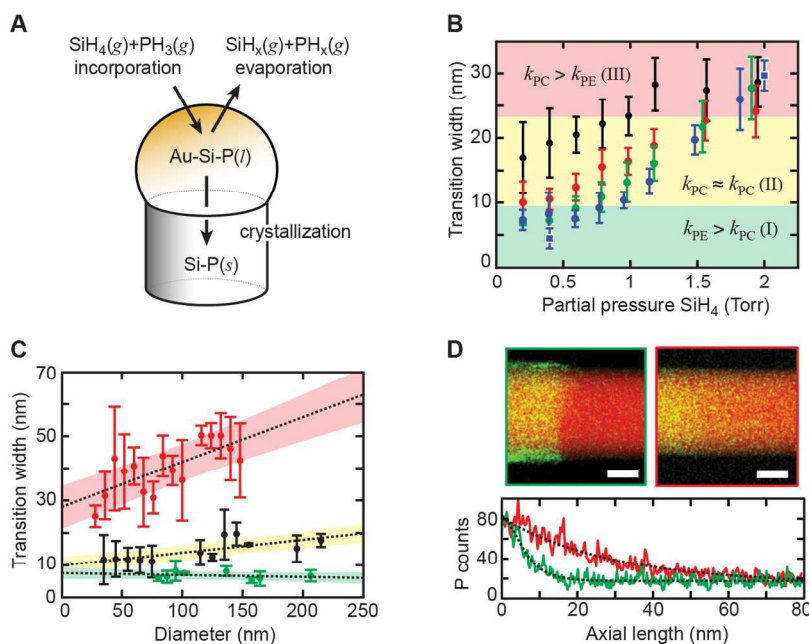


Figure 5. Modeling Dopant Transitions in Si NWs. (A) Illustration of the key processes for describing the time-dependent P concentration in the catalyst and NW: incorporation, evaporation, and crystallization. (B) Plot of transition width relative to partial pressure of SiH₄ for 20 (blue), 40 (green), 60 (red), and 80 (black) Torr total reactor pressure. Blue square data points outlined in white represent transition widths derived from EDS data in panel D. (C) Plot of transition width vs. diameter for NWs grown at a SiH₄ partial pressure of 0.4 Torr and a total reactor pressure of 20 (green) or 80 (black) Torr, as well as a SiH₄ partial pressure of 2.0 Torr and a total reactor pressure of 20 Torr. Black dashed lines are the best linear fits to each data set, and shaded areas represent one standard deviation error in the fit. (D) EDS images (top) and plot of relative atomic counts vs. axial length (bottom) for NWs grown at a SiH₄ partial pressure of 0.4 Torr (left, green) and 2.0 Torr (right, red) at a total reactor pressure of 20 Torr,

with growth rates of ~100 and ~500 nm/min, respectively. Adapted with permission from reference 16. Copyright 2014 American Chemical Society.

In order to understand the abruptness of the dopant transitions, we expanded the kinetic analysis of VLS growth presented above to include P dopants.¹⁶ As illustrated in Figure 5A, in addition to the three microscopic processes of incorporation, evaporation, and crystallization for Si species, we also consider the corresponding processes for P species. The complete kinetic analysis¹⁶ produces a transition width, λ , between n-type and intrinsic sections of:

$$\lambda = \frac{k_c \phi_{Si}}{3(2k_{PE} + k_{PC})} D, \quad (4)$$

where k_{PC} is the rate constant for P crystallization, k_c is the rate constant for Si crystallization, k_{PE} is the rate constant for P evaporation, ϕ_{Si} is the volume fraction of Si in the catalyst, and D is diameter of the catalyst. The factors of 2 and 3 arise from the assumption that the liquid catalyst is hemispherical with a diameter equal to the solid NW diameter. Equation 4 predicts the transition width will scale linearly with diameter D , as expected for the reservoir effect. However, the abruptness is also affected by the pre-factor in equation 4, which is determined by the rate constants k_{PC} , k_c , and k_{PE} . To understand the absence of the reservoir effect under optimal ENGRAVE synthetic conditions, we considered the limiting behavior of these rate constants.

The limits of equation 4 were examined under the assumptions that k_c and ϕ_{Si} were non-zero (*i.e.* the wire is growing and the catalyst is a liquid alloy). First, for synthetic conditions where $k_{PC} \gg k_{PE}$, the transition width becomes:

$$\lambda = \frac{k_c \phi_{Si}}{3k_{PC}} D = \frac{1}{3} \beta \phi_{Si} D, \quad (5)$$

where $\beta = k_c / k_{PC}$ is the segregation coefficient for crystallization of Si and P in the NW (*i.e.* the ratio of P concentration in the liquid to P concentration in the NW). In this limit, the transition width is linearly dependent on the NW diameter, and the reservoir effect cannot be suppressed. Second, for synthetic conditions where $k_{PE} \gg k_{PC}$ the transition width becomes:

$$\lambda = \frac{k_c \phi_{Si}}{6k_{PE}} D . \quad (6)$$

In this limit, λ goes to zero if $k_{PE} \gg k_c$, and the reservoir effect is fully suppressed.

As depicted in Figures 5B and 5C, we measured the transition width of etched NWs grown under a range of synthetic conditions, including NW diameter, growth rate (*i.e.* SiH₄ partial pressure), and total reactor pressure, in order to explore the predictions of the kinetic model developed above. We observe three distinct regions, labeled as I, II, and III in Figure 5B and color coded green, yellow, and red, respectively, in Figures 5B-C. The first region (I; green) corresponds to low total pressures (<40 Torr) and relatively slow growth rates (<300 nm/min). The transition widths in this region are abrupt (<10 nm) and diameter independent. The second region (II; yellow) corresponds to low pressures with intermediate growth rates and high pressures with low growth rates. These synthetic conditions produce a broadened transition (~10-25 nm) that scales linearly with NW diameter. The third region (III; red) corresponds to high NW growth rates at intermediate to high pressures. The transitions in this region are broad (>30 nm) and diameter-dependent. As shown in Figure 5D, these results were confirmed by high resolution EDS maps collected from region I (left image and green trace) and region III (right image and red trace), which produce transition widths of ~4 and ~30 nm, respectively.

The three regions shown in Figure 5 can be understood from the limits of the

kinetic analysis. Region III corresponds to a regime where P evaporation is slow and P crystallization dominates (equation 5), which produces broadened transitions. Region II corresponds to synthetic conditions where the rate constants for P evaporation and crystallization are similar in magnitude (equation 4). Finally, region I corresponds to synthetic conditions where P evaporation is the dominant microscopic process (equation 6). The relatively low pressures and growth rates in region I favor evaporation of P from the catalyst and allow the liquid catalyst to rapidly achieve equilibrium with the gas phase upon removal of the P precursor, which produces abrupt transitions in the NW.

Outlook and Summary

In this Highlight, we have reviewed our recent progress on understanding the microscopic processes and mechanistic details that underpin VLS NW growth and modulation doping. The combination of experimental measurements over a broad set of synthetic conditions and detailed kinetic modeling permit the choice of optimal synthetic conditions to design ENGRAVE nanostructures with sub-10 nm morphological features. We expect the analyses and processes presented here to be generalizable to many classes of NWs grown by a VLS mechanism. For instance, other Si-based material systems, such as B-doped Si and Si-Ge alloys, have been shown to resist etching in aqueous KOH solution. However, these materials will require careful consideration of synthetic conditions to avoid vapor-solid overcoating on the NW surface^{43, 44} and, for B-doped Si, to achieve sufficiently high B concentrations that will serve as an etch stop.^{45, 46} In addition, alternate etching techniques can be considered. For example, Ge-rich portions of SiGe NWs may be selectively removed using a gas-phase HCl etch.⁴⁷ Moreover, the ENGRAVE technique is not necessarily limited to group IV materials. The etch rate of

III-V materials in a bromine wet etch is known to depend on the group V element,⁴⁸ and extending ENGRAVE to III-V materials would enable a variety of applications that utilize the direct bandgap of most III-V semiconductors.

The ENGRAVE process allows the rational design of nanostructures with morphologies tailored to address specific scientific and technological challenges. Several proof-of-principle applications have already been demonstrated, such as bottom-up resistive switches and plasmonic antennae.¹³ We anticipate the ENGRAVE technique can be broadly applied to many areas of nanotechnology, including nanoelectromechanical systems, field-effect transistors, nanophotonics, solid-state memory, thermoelectrics, and biological interfaces.¹⁴

Corresponding Author

*Email: jfcahoon@unc.edu

Acknowledgments

We acknowledge primary support of this research by the National Science Foundation (NSF) through grant DMR-1308695. C.W.P acknowledges a NSF graduate research fellowship, and J.F.C. acknowledges a Packard Fellowship for Science and Engineering.

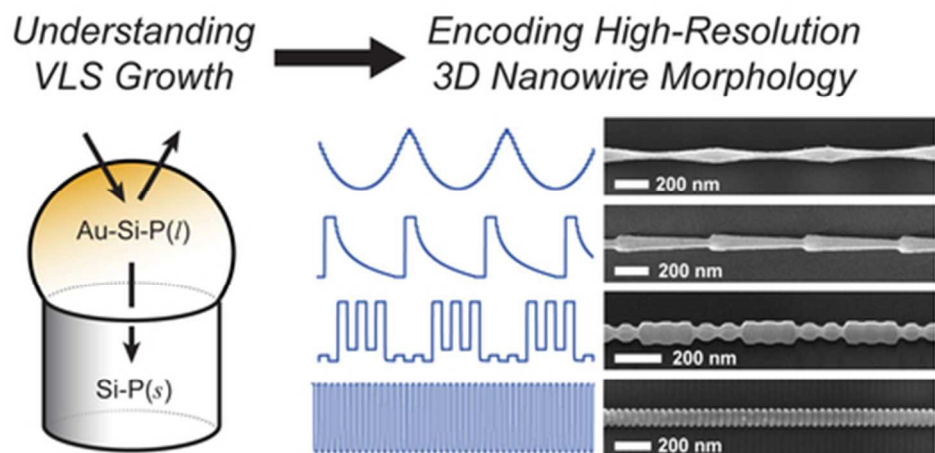
References

1. P. B. Deotare, M. W. McCutcheon, I. W. Frank, M. Khan and M. Lončar, *Appl. Phys. Lett.*, 2009, **94**, 121106.
2. L. Novotny and N. van Hulst, *Nat. Photonics*, 2011, **5**, 83-90.
3. C. M. Lieber, *MRS Bull.*, 2003, **28**, 486-491.
4. P. Yang, R. Yan and M. Fardy, *Nano Lett.*, 2010, **10**, 1529-1536.

5. A. I. Hochbaum and P. Yang, *Chem. Rev.*, 2010, **110**, 527-546.
6. T. J. Kempa, R. W. Day, S.-K. Kim, H.-G. Park and C. M. Lieber, *Energy Environ. Sci.*, 2013, **6**, 719-733.
7. X. Zhang, C. W. Pinion, J. D. Christesen, C. J. Flynn, T. A. Celano and J. F. Cahoon, *J. Phys. Chem. Lett.*, 2013, **4**, 2002-2009.
8. F. Qian, Y. Li, S. Gradečak, D. Wang, C. J. Barrelet and C. M. Lieber, *Nano Lett.*, 2004, **4**, 1975-1979.
9. M. Law, D. J. Sirbuly, J. C. Johnson, J. Goldberger, R. J. Saykally and P. D. Yang, *Science*, 2004, **305**, 1269-1273.
10. Y. Cui, Q. Q. Wei, H. K. Park and C. M. Lieber, *Science*, 2001, **293**, 1289-1292.
11. A. I. Boukai, Y. Bunimovich, J. Tahir-Kheli, J. K. Yu, W. A. Goddard, 3rd and J. R. Heath, *Nature*, 2008, **451**, 168-171.
12. A. I. Hochbaum, R. Chen, R. D. Delgado, W. Liang, E. C. Garnett, M. Najarian, A. Majumdar and P. Yang, *Nature*, 2008, **451**, 163-167.
13. J. D. Christesen, C. W. Pinion, E. M. Grumstrup, J. M. Papanikolas and J. F. Cahoon, *Nano Lett.*, 2013, **13**, 6281-6286.
14. J. D. Christesen, C. W. Pinion, D. J. Hill, S. Kim and J. F. Cahoon, *J. Phys. Chem. Lett.*, 2016, In press.
15. C. W. Pinion, D. P. Nenon, J. D. Christesen and J. F. Cahoon, *ACS Nano*, 2014, **8**, 6081-6088.
16. J. D. Christesen, C. W. Pinion, X. Zhang, J. R. McBride and J. F. Cahoon, *ACS Nano*, 2014, **8**, 11790-11798.
17. G. A. Bootsma and H. J. Gassen, *J. Cryst. Growth*, 1971, **10**, 223-234.
18. J. Kikkawa, Y. Ohno and S. Takeda, *Appl. Phys. Lett.*, 2005, **86**, 123109.
19. S. Kodambaka, J. Tersoff, M. C. Reuter and F. M. Ross, *Phys. Rev. Lett.*, 2006, **96**, 096105.
20. K.-K. Lew and J. M. Redwing, *J. Cryst. Growth*, 2003, **254**, 14-22.
21. H. Schmid, M. T. Björk, J. Knoch, H. Riel, W. Riess, P. Rice and T. Topuria, *J. Appl. Phys.*, 2008, **103**, 024304.
22. V. Schmidt, J. V. Wittemann and U. Gosele, *Chem. Rev.*, 2010, **110**, 361-388.
23. A. Haruta, *Chem. Rec.*, 2003, **3**, 75-87.

24. H. Tsunoyama, H. Sakurai and T. Tsukuda, *Chem. Phys. Lett.*, 2006, **429**, 528-532.
25. H. Y. Hui and M. A. Filler, *Nano Lett.*, 2015, **15**, 6939-6945.
26. H. Wang, L. A. Zepeda-Ruiz, G. H. Gilmer and M. Upmanyu, *Nat. Commun.*, 2013, **4**, 1956.
27. V. Dubrovskii, N. Sibirev, G. Cirlin, I. Soshnikov, W. H. Chen, R. Larde, E. Cadel, P. Pareige, T. Xu, B. Grandidier, J. P. Nys, D. Stievenard, M. Moewe, L. Chuang and C. Chang-Hasnain, *Phys. Rev. B*, 2009, **79**, 205316.
28. V. G. Dubrovskii, *Tech. Phys. Lett.*, 2013, **39**, 157-160.
29. E. I. Givargizov, *J. Cryst. Growth*, 1975, **31**, 20-30.
30. V. Schmidt, S. Senz and U. Gösele, *Phys. Rev. B*, 2007, **75**, 045335.
31. D. Shakthivel and S. Raghavan, *J. Appl. Phys.*, 2012, **112**, 024317.
32. I. Amit, U. Givan, J. G. Connell, D. F. Paul, J. S. Hammond, L. J. Lauhon and Y. Rosenwaks, *Nano Lett.*, 2013, **13**, 2598-2604.
33. T. E. Clark, P. Nimmatoori, K. K. Lew, L. Pan, J. M. Redwing and E. C. Dickey, *Nano Lett.*, 2008, **8**, 1246-1252.
34. F. M. Ross, *Rep. Prog. Phys.*, 2010, **73**, 114501.
35. C. Y. Wen, M. C. Reuter, J. Bruley, J. Tersoff, S. Kodambaka, E. A. Stach and F. M. Ross, *Science*, 2009, **326**, 1247-1250.
36. Y. Wu, R. Fan and P. Yang, *Nano Lett.*, 2002, **2**, 83-86.
37. M. Amato, M. Palummo, R. Rurali and S. Ossicini, *Chem. Rev.*, 2014, **114**, 1371-1412.
38. K. A. Dick, J. Bolinsson, B. M. Borg and J. Johansson, *Nano Lett.*, 2012, **12**, 3200-3206.
39. M. Hilse, M. Ramsteiner, S. Breuer, L. Geelhaar and H. Riechert, *Appl. Phys. Lett.*, 2010, **96**, 193104.
40. K. Hiruma, M. Yazawa, T. Katsuyama, K. Ogawa, K. Haraguchi, M. Koguchi and H. Kakibayashi, *J. Appl. Phys.*, 1995, **77**, 447-462.
41. B. J. Ohlsson, M. T. Björk, A. I. Persson, C. Thelander, L. R. Wallenberg, M. H. Magnusson, K. Deppert and L. Samuelson, *Phys. E*, 2002, **13**, 1126-1130.

42. D. E. Perea, E. R. Hemesath, E. J. Schwalbach, J. L. Lensch-Falk, P. W. Voorhees and L. J. Lauhon, *Nat. Nanotechnol.*, 2009, **4**, 315-319.
43. L. Pan, K. K. Lew, J. M. Redwing and E. C. Dickey, *J. Cryst. Growth*, 2005, **277**, 428-436.
44. P. Gentile, A. Solanki, N. Pauc, F. Oehler, B. Salem, G. Rosaz, T. Baron, M. Den Hertog and V. Calvo, *Nanotechnology*, 2012, **23**, 215702.
45. H. Schmid, C. Bessire, M. T. Bjork, A. Schenk and H. Riel, *Nano Lett.*, 2012, **12**, 699-703.
46. R. A. Schlitz, D. E. Perea, J. L. Lensch-Falk, E. R. Hemesath and L. J. Lauhon, *Appl. Phys. Lett.*, 2009, **95**, 162101.
47. Y. Bogumilowicz, J. M. Hartmann, R. Truche, Y. Campidelli, G. Rolland and T. Billon, *Semicond Sci. Tech.*, 2005, **20**, 127-134.
48. C. Kallesoe, K. Molhave, K. F. Larsen, D. Engstrom, T. M. Hansen, P. Boggild, T. Martensson, M. Borgstrom and L. Samuelson, *J. Vac. Sci. Technol. B*, 2010, **28**, 21-26.



39x19mm (300 x 300 DPI)